Aerospace Science and Technology 138 (2023) 108361

Contents lists available at ScienceDirect

Aerospace Science and Technology

journal homepage: www.elsevier.com/locate/aescte

A trade-off analysis between lateral/directional stability and radar cross section requirements of an air-to-air combat airframe

David Bacci [a,*], Ioannis Vagias [b]

[a] Oxford Thermofluids Institute, University of Oxford, Osney Mead, OX2 0ES, United Kingdom
[b] Cranfield Defence and Security, Defence Academy of the UK, Shrivenham, SN6 8LA, United Kingdom

ARTICLE INFO

Article history:
Received 16 December 2022
Received in revised form 5 April 2023
Accepted 24 April 2023
Available online 29 April 2023
Communicated by Tsourdos Antonios

ABSTRACT

Numerical aerodynamic and radar analyses were conducted on 3 low-radar cross-section airframes, derived from the AVT-183 diamond wing. The geometries were developed by adding different configurations of vertical stabilators, to improve lateral and directional characteristics at high angles of attack whilst minimising the deterioration of radar signature characteristics. The analyses were conducted at a Mach number of 0.30, with angle of attack varying between 0 deg to 30 deg and angle of sideslip varying from 0 deg to 6 deg. Monostatic radar cross-section analysis was conducted in L and X bands. The study explored the trade-off between radar signature control (RCS) and the spin/departure requirements typical of a modern combat aircraft designed for air-superiority. Several of the proposed configuration were shown to improve both lateral and directional stability, whilst maintaining acceptable RCS.

© 2023 The Author(s). Published by Elsevier Masson SAS. This is an open access article under the CC BY license (http://creativecommons.org/licenses/by/4.0/).

1. Introduction

Design requirements of modern and future combat aircraft are strongly influenced by the necessity to control the radar cross section (RCS). This is typically obtained by planform alignment (concentrating radar returns into narrow directions), minimising protuberances, avoiding corner angles and flat fuselage sides, avoiding cylindrical fuselage design, and reducing/eliminating vertical and horizontal empennages. These aspects favoured the adoption of blended-wing-body (BWB) and flying wings designs, such as the Northrop-Grumman B-2, X-47A, X-47B, BAE Systems Taranis, Sukhoi S-70, Dassault nEuron, and Boeing X-45. All these platforms have a common design philosophy, where RCS reduction strongly influences the aerodynamic shape. Furthermore, they are all limited to maximum velocities of transonic (or lower) Mach number and have airframes designed for interdiction and ISTAR roles, rather than for air superiority.

The design of an air dominance aircraft is influenced by manoeuvrability. Fighter agility metrics are typically classified through "power agility" and "pointing agility" [1], [2]. Power agility is related to the rate of change of specific excess power and are typically tuned by carefully balancing engine thrust and airframe drag at combat speeds ranging from subsonic to supersonic. Pointing agility is the capacity of the aircraft to orient the velocity vector spatially, extending the flight envelope at high incidence[1] and side-slip angles [3]. Typical combat engagements are divided into two phases: beyond visual range (BVR) and within visual range (WVR). In the BVR phase, long-range, radar-guided missiles are used, and the aircraft manoeuvring requirements to meet the modern weapons dynamic launch zone (DLZ) are not too demanding. Nevertheless, if fired upon, the situation can change and even in a BVR scenario the aircraft may have to manoeuvre abruptly (i.e. achieving full load-factor capabilities) to evade oncoming missiles. In the WVR scenario, all-aspect IR-guided short-range missiles and air-to-air gunnery dominate. All-aspect IR-guided missiles can be fired from any target aspect angle if their boresight is pointed within the dynamic launch zone of the weapon. This implies the advantage of a point-first capability, meaning the fight would be dominated by transient load-factor or lift-limited manoeuvres.[2] Under such circumstances, the capability of the combat aircraft to quickly manoeuvre is pivotal. The airframe will rapidly achieve high angle of attack values - typically of more than 12 deg. Consequently, the airframe must be fully controllable at these extreme flight conditions in both the longitudinal and lateral/directional directions. The airframe manoeuvring limit is therefore a key feature in all engagement phases. The factors, defining this limit, change

[1] Also known as angle-of-attack.
[2] Knowledge of the use of all-aspect missile by the adversary implies that the attacker might use the maximum instantaneous performance as a defensive tool as well.

* Corresponding author.
E-mail address: david.bacci@eng.ox.ac.uk (D. Bacci).

https://doi.org/10.1016/j.ast.2023.108361
1270-9638/© 2023 The Author(s). Published by Elsevier Masson SAS. This is an open access article under the CC BY license (http://creativecommons.org/licenses/by/4.0/).

Nomenclature

α	angle of attack	deg
β	angle of sideslip	deg
U_∞	free stream air velocity	m/s
ρ_∞	free stream air density	kg/m^3
p_∞	free stream air pressure	Pa
q_∞	free stream dynamic pressure. [Pa]	$\left(=0.5\cdot\rho_\infty\cdot U_\infty^2\right)$
M_∞	free stream Mach number	
U	flow velocity	m/s
l	reference length	m
ν	kinematic viscosity	m^2/s
Re	Reynolds number	$=Ul/\nu$
P_d	power density	W/m^2
S	wing reference area	m^2
c_{ref}	reference chord	m
b_{ref}	reference span	m
S_{vt}	vertical tail reference area	m^2
$c_{vt_{ref}}$	vertical tail reference chord	m
L	lift	N
D	drag	N
E	aerodynamic efficiency	$=L/D$
C_L	lift coefficient	$=L/q_\infty S$
C_D	drag coefficient	$=D/q_\infty S$
C_Y	side force coefficient	$=Y_b/q_\infty S$
C_l	roll moment coefficient	$=L_b/q_\infty S b_{ref}$
C_m	pitch moment coefficient	$=M_b/q_\infty S c_{ref}$
C_n	yaw moment coefficient	$=N_b/q_\infty S b_{ref}$
$C_{m\alpha}$	pitch moment coefficient derivative respect to angle of attack [1/rad]	$(=\partial C_m/\partial\alpha)$
$C_{l\beta}$	roll moment coefficient derivative respect to angle of sideslip [1/rad]	$(=\partial C_l/\partial\beta)$
$C_{n\beta}$	yaw moment coefficient derivative respect to angle of sideslip [1/rad]	$(=\partial C_n/\partial\beta)$
$\vec{x}_{cg}$	centre of gravity position in construction axis system	m
$\vec{x}_{ac}$	aerodynamic centre position in construction axis system	
$\vec{I}$	inertia tensor in body axes system	kg m^2
$\vec{x}_{0w}$	wing aerodynamic centre position in construction axis system	m
$\vec{x}_{0vt}$	vertical tail aerodynamic centre position in construction axis system	m
l_{vt}	vertical tail reference length [m]	$\left(=\left\lvert x_{0w_1}-x_{0vt_1}\right\rvert\right)$
η_{vt}	vertical tail volume coefficient	$(=l_{vt}S_{vt}/b_{ref}S)$
R_D	detection range	n.mi
σ	radar cross section	m^2
f	frequency	Hz
λ	Wavelength	m
γ	azimuth	deg
θ	elevation	deg

Subscripts

∞	free-stream conditions
b	body axis system
c	construction axis system
w	wind axis system
1, 2, 3	vector components in x, y, z direction

Acronyms

FEM	Finite Element Method
IE	Integral Equation Technique (3D Method of Moments)
ISTAR	Intelligence, Surveillance, Targeting, Acquisition and Reconnaissance
SBR-PO	Shooting Bouncing Ray-Physical Optics

according to the flight speed. Indeed, in the transonic and supersonic regimes where the dynamic pressure is high, maximum manoeuvring capacities are typically fixed by structural limits relating to the maximum structural load factor, flutter, and buffeting that are achieved at low-to-medium angles of attack. Conversely, at subsonic speeds, where the dynamic pressure is lower, it is the maximum controllable angle of attack that typically defines the manoeuvring limit.

Analysis of future air combat scenarios might rank manoeuvring in second place, as the developments in air-to-air missile technology, on-board fire control avionics, coupled with low-RCS will dictate that engagements will mainly be conducted in BVR without the opponent having the time or capability to fire back [4], [5]. Nevertheless, considering the advancement of electronic warfare (EW), coupled with the global availability of stealth aircraft design, there is a strong possibility that even a modern low-RCS airframe will have to perform hard manoeuvring either to avoid oncoming BVR missiles or due to moving rapidly to WVR engagement as both sides develop the capability to evade long-range shots.

In recent years, there has been extensive research on Unmanned Combat Aerial Vehicle (UCAV) concepts with vigorous signature control requirements; this involved the adoption of delta, diamond, and lambda wing planform configurations, coupled with blended wing body architectures. The design challenges presented by these aerodynamic configurations have necessarily required exploration. Particular attention has been given to the aspect of flight stability in both the longitudinal and lateral channels. Whilst manoeuvrability is one of the most important aspects in combat aircraft design [6], other factors can strongly influence the flight path of the aircraft, especially in the low-speed regime, and hence govern the performance requirements for controllability [7], [8]. Asymmetric store conditions and sudden engine failure on multi-engine airframes (especially during take-off and climb) are all critical aspects that require adequate mitigating controls to be in-place [6], [9–11], and which, if not properly addressed, can lead to dangerous situations including flight departure, spins, or complete loss of the aircraft. The application of these design criteria to novel low-signature architectures led to the formation of several NATO Science and Technology Organisation (STO) task groups that addressed the associated design challenges. Most notably, the STO considered how to best achieve manoeuvrability and controllability without the use of vertical and horizontal tailplanes, as a measure to minimize RCS, transferring all the control requirements to conventional trailing and leading-edge moving surfaces.

An initial assessment of low-RCS airframe stability and control performance was conducted in the AVT-161 [12] and AVT-201 [13] task groups, and the SACCON (Stability And Control CONfiguration) UCAV model [14–21]. These studies evidenced several configuration deficiencies, principally represented by the non-linear movement and interaction of the wing vortices, leading to severe pitching moment oscillations that impeded steady-state control of the airframe. This prompted the derivation of an improved configuration named MULDICON (MULti-Disciplinary CONfiguration) which was the core study of AVT-251 task group [22]. Part of the objective was the design of a suitable control concept. The conclusion was that the best performance could be attained using wingtip-placed split flaps [23–26]. This outcome was considered the most demanding with regard to lateral/directional control during cross-

wind landings. Nevertheless, even if the lateral/directional stability of a fast jet can be handled by the deployment of ailerons and all-moving horizontal tails, the delegation of aerodynamic control to these surfaces diminishes the longitudinal control power, thus reducing the airframe manoeuvrability. These findings indicated that optimisation of aerodynamic performance with RCS signature reduction represents a challenging procedure. In past studies, initial attempts concentrated on the application of RCS fundamentals [27] to aerofoil shaping [28], [29]. These 2D studies indicated that aerofoil RCS (based on frontal aspect) strongly depended on leading-edge radius and shape, but a significantly low radar signature could be achieved without sacrificing transonic performance. Subsequent research allowed the extension of this multidisciplinary problem to 3D shapes and whole aircraft configurations. Such a method was demonstrated by Lee, et al. [30] who used an evolutionary algorithm for aerofoil selection and wing planform design to optimise performance and reduce RCS for a transonic UCAV configuration. Other studies expanded the multidisciplinary design optimisation (MDO) adding structural [31], [32] and stability [33], [34] requirements. More recent research continued to explore both aerodynamic and stealth optimisation via different algorithms whilst still concentrating on reconnaissance and ground attack airframes and mission profiles [35], [36]. Common findings indicated that optimal performance was achieved through reducing the leading edge radius [37], [38]. A recent paper from Shao et al. [39] demonstrated how fluidic actuators could be used to maintain sufficient control requirements whilst not significantly degrading RCS performance. However, at elevated angles of attack, bleeding from the engine feeding the fluidic system, could cause a loss in engine thrust of up to 5%.

All these MDO studies concentrated mainly on planform shape, aerofoil shape, and general configurations not involving vertical empennages. Additionally, the configuration and mission profiles explored were typical of reconnaissance and ground attack roles, rather than air superiority. Little attention to-date has been given to exploring the trade-offs of an air-to-air combat airframe with augmented manoeuvring performance in the open literature. It is however, worth noting that current 5th generation fighters (Lockheed Martin F-22, F-35, Sukhoi Su-57, Su-75, Chengdu J-20, Shenyang J-31, and Turkish Aerospace Industries MMU) have been designed (or are under the final stage of development) as multi-role platforms that can achieve air dominance at short, medium and long ranges. Similarly, future 6th generation proposals (BAE Systems Tempest, Dassault/Airbus FCAS) appear to retain vertical empennages. Hence vertical tails cannot be removed for some future combat aircraft typology, and a trade-off design will have to be conducted to satisfy lateral and directional characteristics without excessively compromising the RF low observable (LO) characteristics.

This paper lays out a study to determine the trade-off between RCS and the aerodynamic requirements of lateral/directional controllability, thereby addressing the gap that exists in the literature between these two design requirements in the sub-domain of air dominance airframes. The present work seeks to explore the effectiveness of 3 vertical empennage configurations installed on a low-RCS airframe, the AVT-183 diamond wing with the aim to provide an initial qualitative and qualitative analysis of how such an airframe can increase the lateral-directional characteristics without excessive detrimental effects on the signature. This configuration was developed to explore blunt leading-edge vortex separations as a direct consequence of the SACCON airframe [40,41]. The rationale behind the selection of this airframe was the presence of both radar signature and aerodynamic characteristics typical for current and future air superiority fighters [23], [24–26].

The derived airframes, incorporating different vertical tail planforms, were developed including design aspects such as edge alignment and cant angle, which are typical for radar signature control. Monostatic RCS and aerodynamic analysis were conducted using Computational Electromagnetic Methods (CEM) and Computational Fluid Dynamics (CFD), respectively. The effectiveness of the different designs was tested at a subsonic Mach number of 0.3, typical of a high angle of attack flying position in a close-range dogfight scenario [43], where the lateral/directional requirements are most demanding for a manoeuvring aircraft. The analysis criterion was dictated by a trade-off between RCS in "L" and "X" bands, and the static lateral/directional capabilities of the airframes.

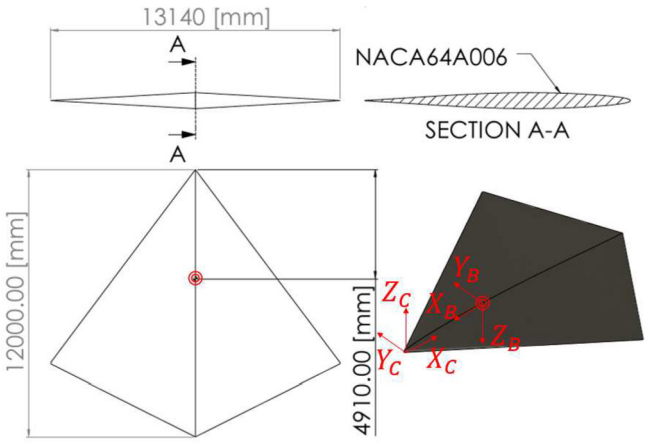

Fig. 1. Construction and body axes systems and configuration v_0 overall layout.

2. Methodology

2.1. Geometry

Initially, the present study assessed the diamond-shaped AVT-183 airframe, with a leading-edge sweep of 53 deg and trailing-edge sweep of −26.5 deg. The wing section utilised was the NACA 64A006 aerofoil [44], [45]. The original wind tunnel model used in the AVT-183 task group was scaled by a factor of 10 to replicate the typical dimensions of an aircraft. The wing tip was locally modified, and a chord of 150 mm was introduced to provide a shape more representative of real configurations where both manufacturing and structural considerations preclude zero taper (corresponding to a pointed tip). The final (upscaled) baseline configuration (Fig. 1) was labelled $v0$.

From this basic shape, 3 vertical tails arrangements were developed. The core design requirement was the preservation of alignment with the wing planform. The cant angle was fixed at 45 degrees (positive or negative according to the developed geometry). The root chord was always placed inside the wing perimeter, whilst the aerofoil used was the same at that of the NACA 64A006 wing.

Although general sizing methods do exist ([46–50]), several degrees of freedom were present in the design of the vertical tails. The driving factor in empennage sizing was the volume coefficient (η_{vt}). Historical trends for combat jets ([46,47,49]) indicate values between 0.06 and 0.07. However, configurations with values as low as 0.04 and as high as 0.12 have been utilised ([42,48,50,51]). To minimise the increase in RCS, it was then decided to opt for the lowest admissible value of η_{vt}. Consequently, all configurations were designed to have a tail volume coefficient of 0.04.

The 3 derived airframes, shown in Fig. 2, Fig. 3 and Fig. 4, were respectively labelled v_1, v_2, and v_3. The first geometry (v_1) had two outward canted tails. The outward spacing, and root chord size, were a direct consequence of attempting to place the fins as far back as possible whilst maintaining the desired value of

Table 1
Configurations Data.

Parameter	*Units*	v_0	v_1	v_2	v_3
S	m^2	78.84			
c_{ref}	m	8.00			
b_{ref}	m	13.14			
$\overrightarrow{x}_{cg}$	m	[4.91, 0.0, 0.0]			
l_{vt}	m	-	4.07	2.68	5.23
S_{vt}	m^2	-	10.23	15.48	8.08
$c_{vt_{ref}}$	m	-	4.10	3.57	2.21
η_{vt}	–	-	0.04	0.04	0.04
I_{zz}/I_{xx}	–	2.1305	2.1960	1.9497	2.2212

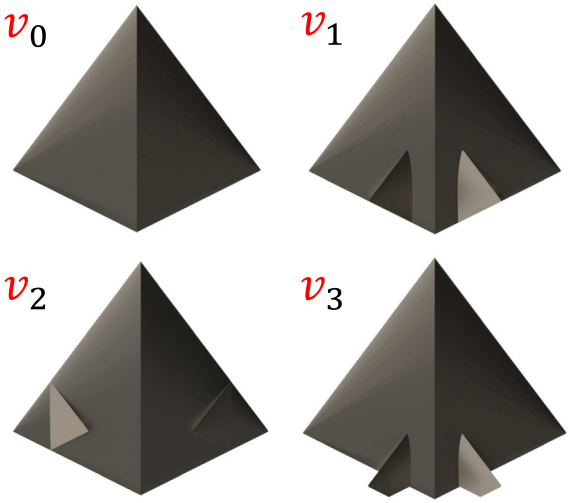

Fig. 2. Geometries analysed. Top view.

η_{vt}. The second geometry (v_2), adopted a quadruple empennage solution, located toward the wing tips, with two fins above and below the wing surface (see Fig. 4-v_2). Finally, the third geometry (v_3) was similar to v_1, with outward canted tails, placed in proximity to the wing's trailing edge. However, in this case, a different shape was selected, with the fins having a V-shaped trailing edge instead of being straight (see Fig. 2-v_3). The derivation of these 3 geometries was not solely a design process governed by tail volume coefficient and planform alignment requirements. The horizontal shape of empennage configuration v_1 was derived to directly resemble the design solution of the Lockheed Martin F22, which in terms of manoeuvrability represents the state of the art for 5th generation fighters. The architecture of v_3 was built to resemble the empennage of BAE Systems Tempest. Finally, v_2 was designed to have high lateral-directional stability when flying at high angles of attack. The decision to cant the tails inward was driven by the consideration of having the dihedral angle (between the tail surface and wing surface) greater than 90 deg to improve the redirection of incident radar waves away from the transmitter/receiver.

The main geometric data for all configurations are summarised below in Table 1. For the calculation of the I_{zz}/I_{xx} ratio, semi-empirical methods ([47,52]) were used, together with the analysis of volume distribution from the CAD models.

2.2. Numerical simulation – computational fluid dynamics

The simulations were performed using ANSYS Fluent 2021R2 CFD code, adopting the SST-$k\omega$ generalised turbulence model ($GEKO$ [53]). The model accounted for a curvature correction term to address common challenges with $k\omega$ turbulence models in dealing with strong swirling flows [54], typically found in the core of delta wing vortices. The turbulence model was adopted as it had

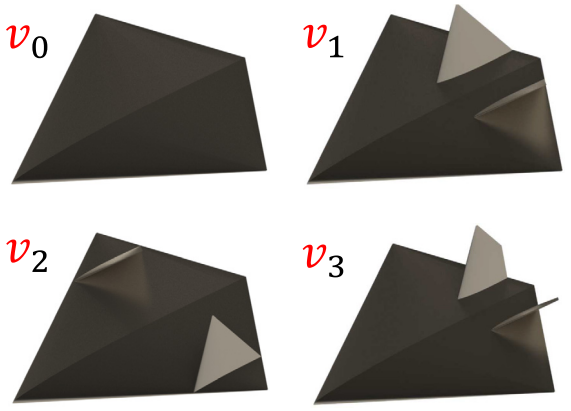

Fig. 3. Geometries analysed. Isometric view.

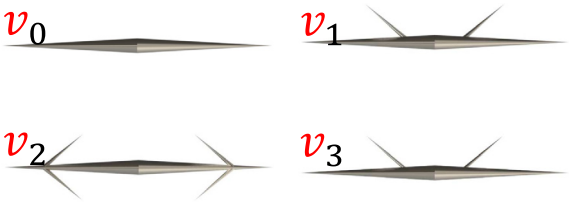

Fig. 4. Geometries analysed. Front view.

previously been demonstrated (when compared with other RANS models) to most accurately capture pressure distributions for such configurations [55], [56].

The mesh utilised unstructured polyhedral-type cells, with 22 layers of prisms cells having a growth ratio of 1.2, and wrapping the viscous surfaces resulting in a y^+ value of unity or less. All solid walls were specified as being adiabatic, with a no-slip velocity condition applied. The computational outer boundary was specified as a far-field, using the modified Riemann invariants condition.

The air was treated as an ideal compressible gas using Sutherland's law for viscosity modelling. Due to the compressible nature of the problem, a pressure-based coupled (in momentum and continuity) solver was used. Non-viscous fluxes were resolved using a second-order centred scheme; viscous fluxes and energy equations were resolved using a second-order upwind scheme; gradients were evaluated using the least squares method.

Data from the AVT-183 wind tunnel (WT) experiments [45] was used to validate the numerical procedure: a geometry similar to the WT model, consisting of a half wing, with a root chord of 1200 mm, was used, applying a symmetry-flow condition in the vertical plane. Three meshes were developed for the half-wing; coarse, medium, and fine with 10e6, 18e6, and 27e6 elements respectively. Longitudinal forces and moments (in terms of lift, drag and pitching-moment coefficients) were compared to experimental data.

The results of mesh validation are shown in Fig. 5. The level of agreement between the medium and fine grids was sufficient to consider that the fine grid produced a grid-converged solution. Accuracy in the prediction of lift, drag, and pitch-moment coefficients was in line with previous computational studies on similar geometries ([41,55–57]).

With the above settings, 400 iterations were required to achieve a residual reduction below 1e-6 for momentum and energy equations, and below 1e-4 for turbulence and continuity equations. To determine the convergence of forces and moments, the Aerodynamic Coefficient Convergence index (C_{CI}) was introduced, and is defined as:

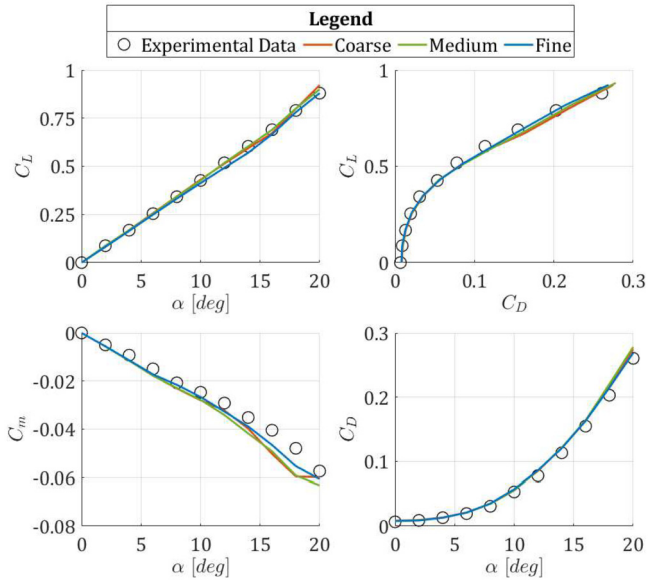

Fig. 5. CFD validation and comparison with experimental data [45].

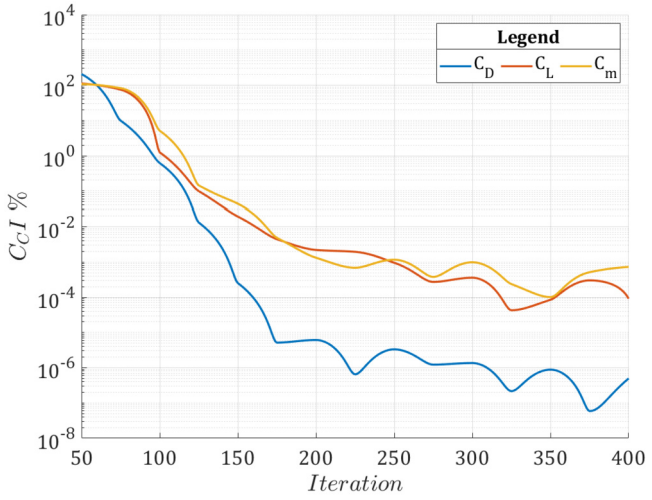

Fig. 6. Aerodynamic coefficient convergence index trend with iterations for the case at zero angle-of-attack. Fine mesh at $\alpha = 20$ deg.

$$C_{CI} = 100 \cdot \left| \frac{C_x^{i+1} - C_x^i}{C_x^i} \right| \tag{1}$$

Here C_x^i is the force (or moment coefficient) at i^{th} iteration, whilst C_x^{i+1} is the value at the successive iteration. As shown in Fig. 6, the selected value of 400 iterations was sufficient to achieve stable C_{CI} values below 1% for both force and moment coefficients, indicating the convergence of the solution.

The computational domains for all other geometries were constructed following the fine-mesh settings. Each configuration was tested at angles of attack ranging from 0 to 30 degrees at 3 degree intervals. At each angle of attack, a sweep in angles of sideslip, from 0 to 6, in intervals of 3 degrees, were performed to calculate the lateral aerodynamic coefficients. This resulted in a total of 33 test points (Table 2) for each geometry. Freestream Mach number was kept constant at a value of 0.3 - a representative value for flight regimes at high angles of attack ([58], [59]). It is typically in the low-speed regime where the adverse phenomena in the lateral and directional channel (spin, departures, nose-slice) are most critical and occur with the highest severity [43,60–62]

Table 2
CFD Test matrix and boundary conditions.

M_∞	p_0 [Pa]	T_0 [K]	α [deg]	β [deg]
0.3	101325	300	0:3:30	0:3:6

Table 3
RCS Test Matrix.

Band	f [GHz]	*Polarisation*	γ [deg]	θ [deg]
X		HH	0:0.5:180	-90:0.5:90
		VV		
L	1.3	HH	0:1:180	–90:1:90
		VV		

2.3. Numerical simulation – radar cross section

Monostatic radar cross-section calculations were conducted using the ANSYS HFSS 2021R2 CEM code, a hybrid FEM/IE/SBR-PO solver. Diffraction is also modelled using PTD (Physical Theory of Diffraction) and UTD (Uniform Theory of Diffraction) methodologies. The RCS was calculated using the far-field assumption. Surfaces were modelled as perfect electric conductors.

Each configuration was analysed at two frequencies, 9.6 GHz, representing a typical operating frequency of an X band tracking and acquisition radar, and 1.3 GHz, a typical operating frequency of an L band long-range surveillance radar. At each band, horizontal (HH) and vertical (VV) polarisation scans were conducted. An RCS database was assembled with scans in azimuth between 0 deg to 180 deg, and scans in elevation between –90 deg to 90 deg. The final test matrix is reported in Table 3.

The numerical procedure was validated using the NASA Almond model [63]. Experimental data were compared to code predictions, at 2 different frequencies, 1.19 GHz and 7 GHz, corresponding respectively to an electrical size (ratio of characteristic length of the object to radar wavelength) of 1.01 and 5.93. The comparison was conducted both in HH and VV polarisations. The results are shown in Fig. 7. At the frequency of 1.19 GHz (Fig. 7-left), the simulations were capable of accurately predicting RCS in both VV and HH polarisations. Similarly, at higher frequency (Fig. 7-right) good agreement with the experimental data was observed at both polarisations.

Mesh convergence was validated for the v_0 geometry in Lband and Xband. Four meshes were developed; coarse, medium, fine and extra-fine, with respective mesh maximum sizes of 0.25, 0.125, 0.1, and 0.05 times the incident wavelength. As shown in Fig. 8 the level of agreement between the fine and extra-fine meshes was sufficient to consider that the fine mesh produced a grid-converged solution.

3. Data analysis procedure

3.1. Aerodynamics

Flight at medium to elevated incidence can give rise to issues such as wing-rock, wing drop, departure, and nose slice [64]. All these phenomena are typically characterised by the inability of the control surfaces to overcome force and moments typical of separated flow. Positive values of the directional derivative (C_{n_β}) and negative values of the lateral derivative (C_{l_β}) represent the starting point for classical stability analyses. However, dynamic response and control effectiveness characteristics also require detailed analysis. The necessary data may not be available during the preliminary design phase, where one or more airframe configurations must be shortlisted. To address this, static-derivative-based dynamic criteria have been developed to provide guidance [65]. A

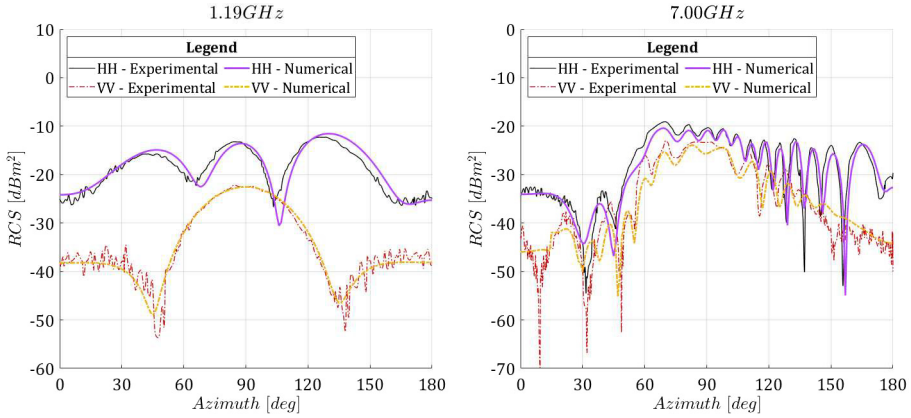

Fig. 7. CEM validation and comparison with experimental data [63].

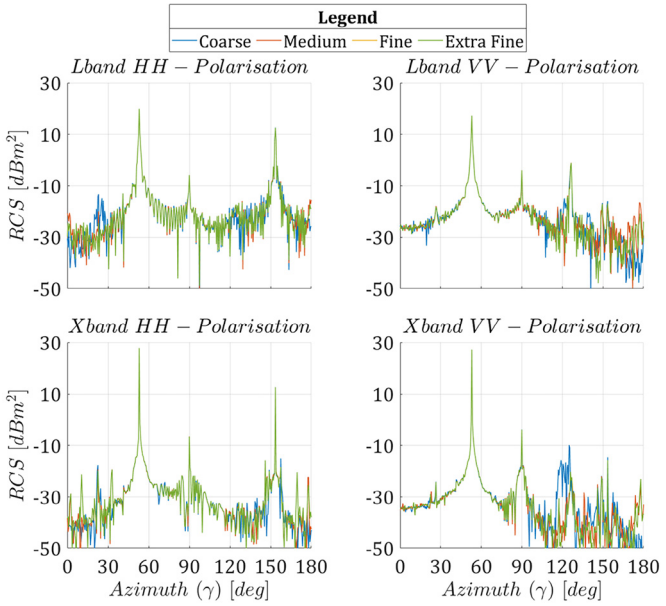

Fig. 8. Mesh refinement study. Full scan in azimuth at zero elevation. Baseline geometry.

good indicator of aircraft departure from controlled flight is the directional stability parameter ($C_{n_{\beta,dyn}}$), defined as:

$$C_{n_{\beta,dyn}} = C_{n_\beta}\cos\alpha - \left(\frac{I_{zz}}{I_{xx}}\right)\cdot C_{l_\beta}\sin\alpha \tag{2}$$

This derivative, if negative, is a sufficient condition for directional divergence. This is an open loop parameter, and in the case of positive values, it must be integrated with other predictors [66]. An additional indicator of eventual departure at high angles of attack is the Lateral Control Departure Parameter (LCDP):

$$LCDP = C_{n_\beta} - C_{l_\beta}K_{AR} \tag{3}$$

$$K_{AR} = \left(\frac{C_{n_{\delta_a}} + \frac{\delta_r}{\delta_a}C_{n_{\delta_r}}}{C_{l_{\delta_a}} + \frac{\delta_r}{\delta_a}C_{l_{\delta_r}}}\right) \tag{4}$$

Here, δ_r and δ_a are the rudder and aileron deflection angles respectively. This parameter must be positive for an airframe to be properly controllable in the lateral/directional axes.

As this study is principally focuses on preliminary design trade-offs, neither ailerons nor rudder geometries were evaluated. The effectiveness of the vertical empennages was measured by examining the derivatives C_{n_β}, C_{l_β}, and $C_{n_{\beta,dyn}}$, and considering $LCDP$ as shown in the Bihrle-Weissman (BW) chart in Fig. 9 [66]. Seven regions are identified for different combinations of $LCDP$ and $C_{n_{\beta,dyn}}$. Class "A" is that deemed optimal and where the aircraft has both excellent lateral and directional characteristics. Moving away from this boundary, the characteristics of the aircraft begin to deteriorate and phenomena such as roll-reversal, and spin departure can be observed when manoeuvring. The theoretical minimum, for an airframe, is to avoid class "B", "C", and "D", which represent areas of complete loss of control. For class "E" and "F" the aircraft would incur weak instabilities but secondary factors (such as aeroelastic or coupling effects) must be investigated to clear the flight envelope. Finally, class "U" is characterised by high directional stability that could be recovered only by a state-of-the-art flight control system design (FCS).

Modern FCS can overcome instabilities and make the aircraft fully controllable even if it is classified as "E", "F", or "U". Nevertheless, during air combat, if control authority is required to overcome a lateral or directional instability, the overall airframe will lose manoeuvring margin as part of the allowable deflection of the control surfaces is engaged in avoiding departures [67]. The outcome will be reduced overall manoeuvrability potential for the airframe. For an air dominance platform, full control must be maintained at a high angle of attack. According to the BW chart, this requires $LCDP$ and $C_{n\beta dyn}$ to lie inside region "A". Each configuration was then evaluated accordingly. The resulting analysis procedure was based on the calculation of $C_{n\beta_{dyn}}$ from CFD analysis. The next step was the calculation of $LCDP$ through Eq. (3) To do so an assumption on K_{ARI} was necessary. There is a theoretical maximum value of this parameter that can be used to avoid control surface saturation in combat engagements. For this study, the maximum allowable K_{ARI} was specified as ±8 based on historical trends highly manoeuvrable combat aircraft that showed excellent control characteristics at high angles of attack [46–49]. Once the $LCDP$ was known, it was possible to determine the class for the airframe under assessment.

3.2. Radar cross section

The calculated radar cross-section was defined as:

$$\sigma = \lim_{R\to\infty}\left(4\pi R^2\frac{P_{d_r}}{P_{d_i}}\right) \tag{5}$$

Here, P_{d_i} is the power density of the incident plane wave and P_{d_r} is the power density of the reflected wave. Obtained data was reported on decibel scale. As such:

$$RCS(\mathrm{dBm^2}) = 10\log_{10}\sigma(\mathrm{m^2}) \tag{6}$$

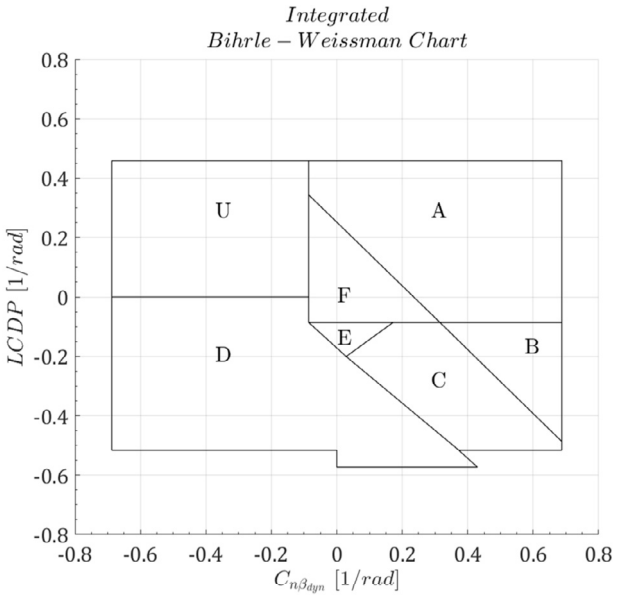

Legend

Class	*Description*
A	Highly departure and spin resistant
B	Spin-resistant, objectionable roll reversals can induce departure and post-stall gyrations
C	Weak spin tendency, strong roll-reversal result in control-induced departure
D	Strong departure, roll reversals and spin tendencies
E	Weak spin tendency, moderate departure and roll reversals, affected by secondary factors
F	Weak departure and spin resistance, no roll reversals, heavily influenced by secondary factors
U	High directional instability

Legend

Class	*Description*
A	Highly departure and spin resistant
B	Spin-resistant, objectionable roll reversals can induce departure and post-stall gyrations
C	Weak spin tendency, strong roll-reversal result in control-induced departure
D	Strong departure, roll reversals and spin tendencies
E	Weak spin tendency, moderate departure and roll reversals, affected by secondary factors
F	Weak departure and spin resistance, no roll reversals, heavily influenced by secondary factors
U	High directional instability

Fig. 9. Integrated Bihrle-Weissman chart.

Units were decibel relative to a square meter. Regarding the sign of azimuth and elevation angles, the relative transforms from construction axes (Fig. 1) were defined as follows (see Fig. 10 for visual reference):

$$\gamma = \tan^{-1}\left(\frac{y_c}{-x_c}\right) \tag{7}$$

$$\theta = \tan^{-1}\left(\frac{\sqrt{x_c^2 + y_c^2}}{z_c}\right) \tag{8}$$

To compare effects in RCS variation between the baseline configuration and the installed airframe vertical tails, a general reference curve, for detection range trend versus target RCS was used (Fig. 11). The assumptions for the derivation of the plot are detailed and described in Knott et al. [68].

Using this figure, it was possible to associate a change in RCS with a relative change in the detection range. The associated metric, termed the "Detection Range Factor" (DRF), was defined as:

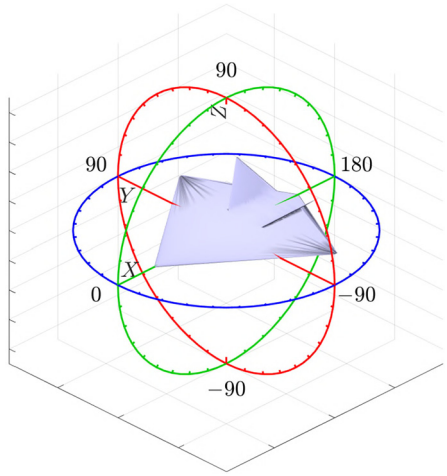

Fig. 10. Positive sign convention for azimuth and elevation angles.

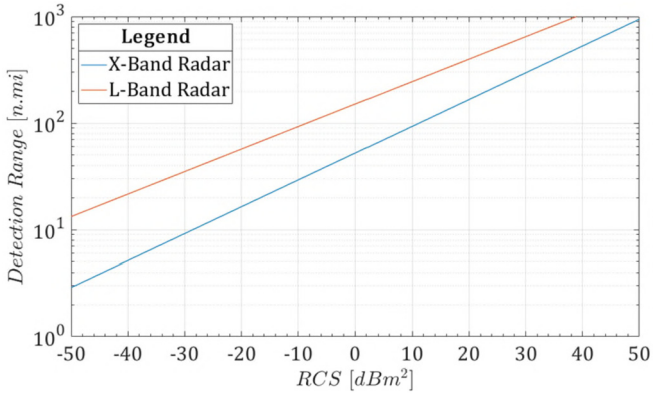

Fig. 11. Typical trend of detection range vs RCS for Lband and Xband Radars. Adapted from Knott, et al. [68].

$$DRF_{v_n} = \frac{R_{D_{v_n}}}{R_{D_{v_0}}} \tag{9}$$

Here, $R_{D_{v_n}}$ is the detection range of configuration v_n ($n = 1, 2, 3$, i.e. one of the derived airframes), whilst $R_{D_{v_0}}$ is the detection range for the baseline geometry. Both values are calculated using the trends depicted in Fig. 11. Thus, a DRF value greater than 1 would correspond to an increase in detection range (and RCS) in comparison to the baseline geometry, whilst a value less than 1 equated to a decrease.

4. Results

The results are presented in three parts. First, an aerodynamic analysis is conducted on the longitudinal and lateral/directional characteristics. The second part presents the effect of vertical tail installation on RCS increase from the baseline geometry. Finally, considerations are derived in terms of the trade-off between low-observability and manoeuvrability requirements.

4.1. The effect of vertical tail on the aerodynamics characteristics

4.1.1. Longitudinal characteristics

The most relevant consequence of the introduction of tailplanes was the deterioration of lift performance. The analysis of the C_L curve (Fig. 12, upper left) indicated that all derived configurations experienced an earlier departure from region of linearity. Additionally, vertical tail introduction reduced the maximum lift coefficient.

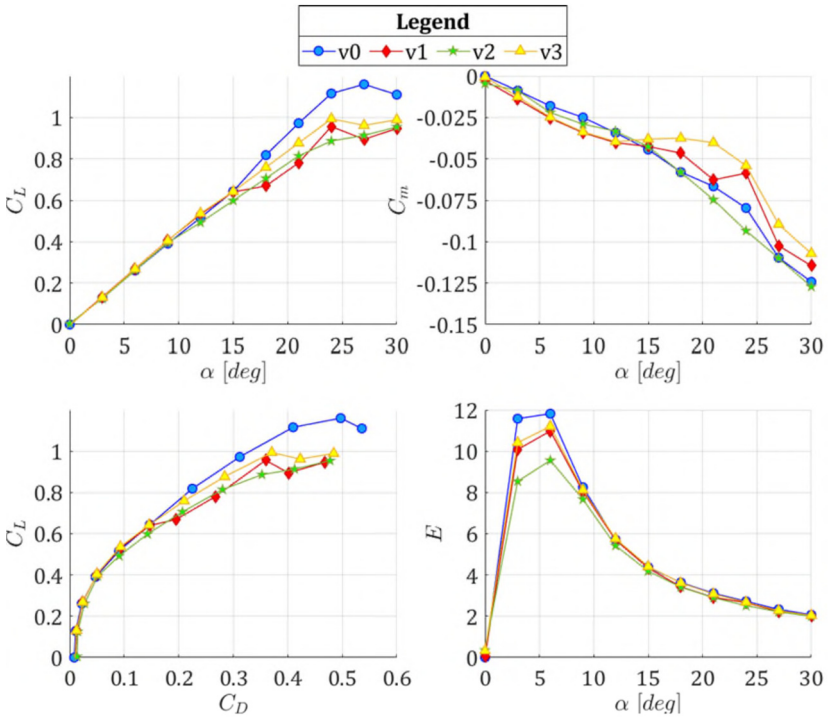

Fig. 12. Longitudinal coefficients trend with angle of attack. β =0 deg.

This effect was explained by inspecting flow characteristics in the stall regime. As shown by the label "A" in Fig. 13, wing vortex trajectory impacted the empennages. This, in turn, influenced the natural evolution of the vortices, moving their burst position upstream when compared to baseline geometry (Fig. 13, label "B").

Tail installation also impacted the drag (Fig. 12, lower) and pitching characteristics (Fig. 12, upper right). This was in line with previous studies assessing the aerodynamic characteristics of low-RCS airframes [69–71]. The derived geometries suffered a decrease in maximum aerodynamic efficiency (Fig. 12, lower right) respectively of −7% for v_1, −19% for v_2 and −5% for v_3. Nevertheless, the location of the maxima remained unchanged with respect to the baseline configuration. Such an effect was correlated to the increase of wetted area represented by the adoption of the empennages, with the associated increase in skin friction.

The trend in the pitch moment of the v_2 configuration was identical to the baseline geometry. In contrast, changes were observed for configurations v_1 and v_3 (Fig. 12, upper right). Configuration v_3 experienced a sudden loss of linearity at α = 12 deg, with a positive value of $C_{m\alpha}$ up to the 21 deg. On the other hand, the tail geometry of v_1, induced a non-linear behaviour as the C_m curve passed the critical value of α = 12 deg. These variations in pitching characteristics were again associated with the mutual interaction between wing vortices (and their breakdown) with vertical empennages.

When compared with the baseline geometry, configuration v_3 demonstrated the lowest decrease in $C_{L_{MAX}}$ and E_{MAX} (−1% and −5% respectively), whilst configuration v_2 registered the highest variations (−4% and −19% respectively). The better performance of v_3 was related to the downstream position of the empennage compared with the other geometries, as it was shown to better decouple the flow structures developed from the tails and wings (Fig. 13, label "A").

4.1.2. Lateral and directional characteristics

Lateral and directional characteristics demonstrated the inherent instability of the baseline configuration across all angles of attacks (see Fig. 14). The introduction of the vertical tails had differing effects according to the specific configuration. Configurations v_1 and v_3 had similar trend up to the critical value of $\alpha = 12deg$. In this range of angle of attack (i.e. from 0 deg to 12 deg) the directional stability ($C_{n\beta}$) assumed a positive value of 0.06 per radian (Fig. 14, lower left). The two airframes were also stable in the lateral channel ($C_{l\beta}$), though in this case the derivative values varied from a minimum of −0.08 per radian to a maximum of −0.02 per radian (Fig. 14, upper right). Past the critical incidence of 12 deg, both v_1 and v_3 experienced an abrupt loss of lateral and directional stability reaching values of zero at α = 15 deg.

Increasing the angle of attack above 15 deg resulted in a condition, for both v_1 and v_3, of being stable directionally but unstable laterally. At post-stall angles of attack, another critical point was identified, corresponding to α = 27 deg. Here both v_1 and v_3 demonstrated instability. Stability was re-established when moving to higher incidences.

Configuration v_2 exhibited a very different trend and was able to remain stable, both laterally and directionally, at all angles of attack.

Lateral and directional derivative trends are reflected through the $C_{n\beta_{dyn}}$ parameter. Once again v_2 was considered stable ($C_{n\beta_{dyn}} > 0$) for the range of angles of attack studied. Configurations v_1 and v_3 were stable up to α = 12 deg. Past this point, they both exhibited unstable behaviour, albeit at varying angles of incidence. For v_1 the instability was observed at α = 15 deg and in the region between α = 24 deg to α = 27 deg. By contrast, for v_3 the instability was observed in the region between α = 15 deg to α = 24 deg, and for $\alpha > 27$ deg.

Flow visualisation (Fig. 15) provided further insight into these critical points, where configurations v_1 and v_3 experienced loss of stability. As shown from labels "B" of Fig. 15, at α = 24 deg and β = 6 deg, wing vortex breakdown was strongly asymmetrical. The observed trend was the leeward vortex bursting further downstream with respect to the windward. Such an observation is associated with laterally unstable behaviour [72] and is a characteristic typical of delta wings [37] (Fig. 15, upper left, label "B"). The presence of a close-placed vertical tail further exacerbated the

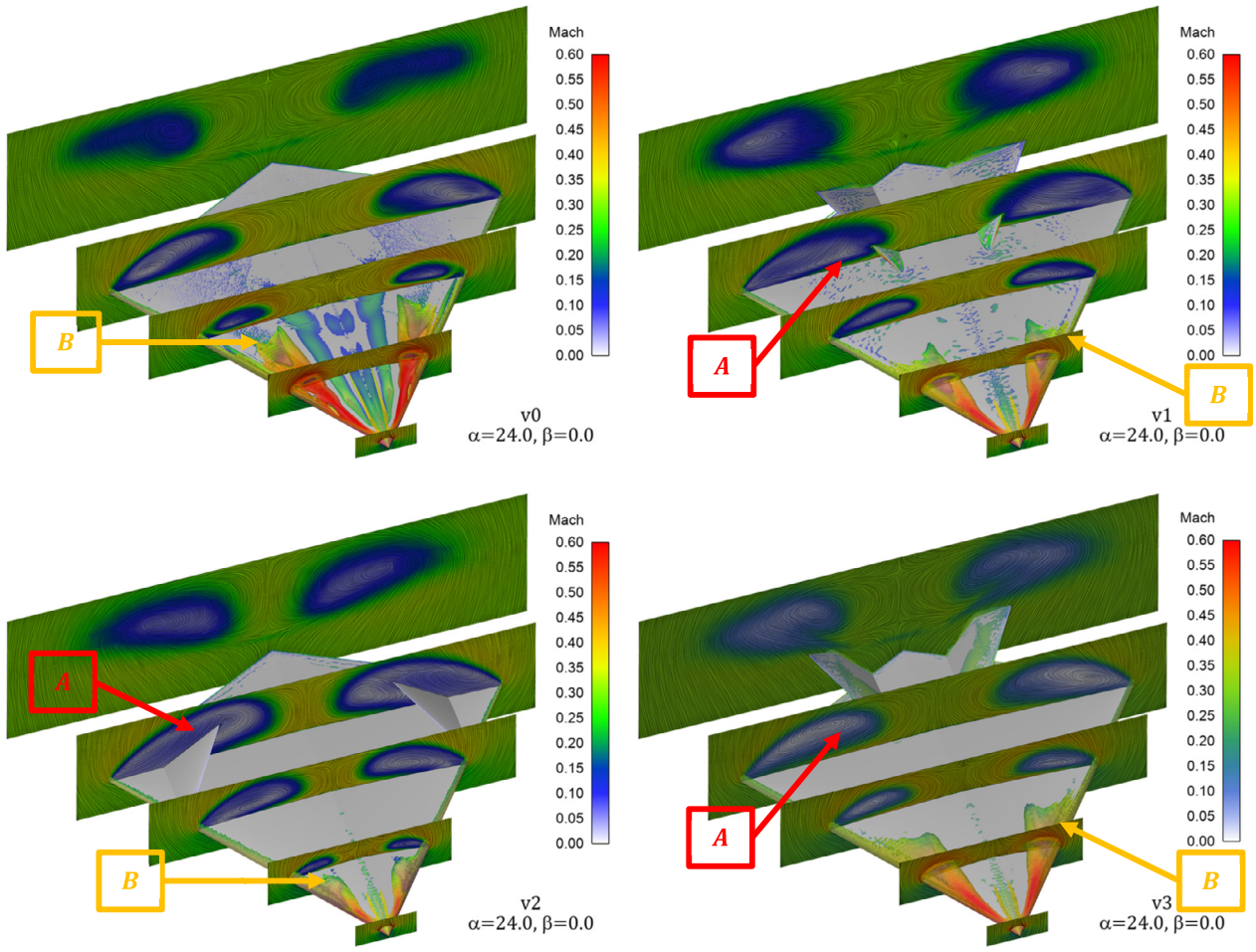

Fig. 13. Flow field comparison at $\alpha = 24\ deg$, and $\beta = 0\ deg$. Planar contours (at different longitudinal positions) of Mach number, and Iso-surface of vorticity. "A label": interaction between vortex wake with vertical empennage. "B label": vortex breakdown position.

mechanism (as in the case of v_1 - Fig. 15, upper right, label "A"). By contrast for v_3 the influence of tails on wing vortices was less pronounced (Fig. 15, lower right, label "A"). This resulted in a less severe loss of stability, at this angle of attack, for v_3 with respect to v_1 as already demonstrated in Fig. 14.

Configuration v_2 showed the same level of interference observed in v_1, between the wing vortices and the vertical empennage (Fig. 15, lower left, label "B"). In this case, the stability was recovered (as shown in the analysis of Fig. 14) by the presence of the lower surface empennages exposed to undisturbed airflow.

The final step of the aerodynamic study was the determination of spin/departure resistance characteristics, according to the WB-chart criteria. The outcome of the analysis is summarised in Table 4 where red letters indicate a flight condition (angle of attack value) where the geometry under exam was not capable to attain class "*A*".

The baseline geometry could not achieve the desired handling characteristics, especially at high angles of attack. Class "*A*" was only achieved in the interval from 6 deg to 9 deg. Outside of this range, the airframe fell into class "*F*". Within the derived geometries, only v_2 could achieve the desired characteristics across the entire angle of attack envelope. Conversely, geometries v_1 and v_3 had issues at high angles of attack. Configuration v_1 achieved class "*A*" up to $\alpha = 18$ deg and at $\alpha = 30$. In the range between $\alpha = 21$ deg to $\alpha = 27$ deg lateral/directional stability was considerably degraded and the class dropped to an "*F*" typology. Configuration v_3 achieved "*A*" class up to $\alpha = 12$ deg. Past this point, an abrupt loss of directional stability degraded the airframe to class

Table 4
Spin/Departure characteristics trend with angle of attack according to Bihrle-Weissman chart (see Fig. 9 for labels description).

Configuration	α [deg]										
	0	3	6	9	12	15	18	21	24	27	30
v_0	F	F	A	A	F	F	F	F	F	F	F
v_1	A	A	A	A	A	A	A	F	F	F	A
v_2	A	A	A	A	A	A	A	A	A	A	A
v_3	A	A	A	A	A	F	A	U	F	F	F

"*F*". It is noteworthy that geometry v_3 had irregular behaviour at these angles of attack. Moving from $\alpha = 15$ deg to $\alpha = 18$ deg the airframe recovered full stability. However, at $\alpha = 21$ deg the lateral and directional characteristics degraded again, moving into the "*U*" boundary. Finally, stability was partially recovered and class "*F*" was resumed ($\alpha \geq 24$ deg).

4.2. The effects of vertical tail on detection range increase

The previous section demonstrated the necessity of the introduction of vertical empennages to enable the baseline geometry to achieve the desired flight mechanics that are typical of highly manoeuvrable combat aircraft. However, in modern combat jets design, radar signature is of great significance and cannot be ignored.

This section explores the quantitative effect of RCS deterioration when vertical tails are incorporated into the baseline geometry. Analysis of data is divided between Lband and Xband. The

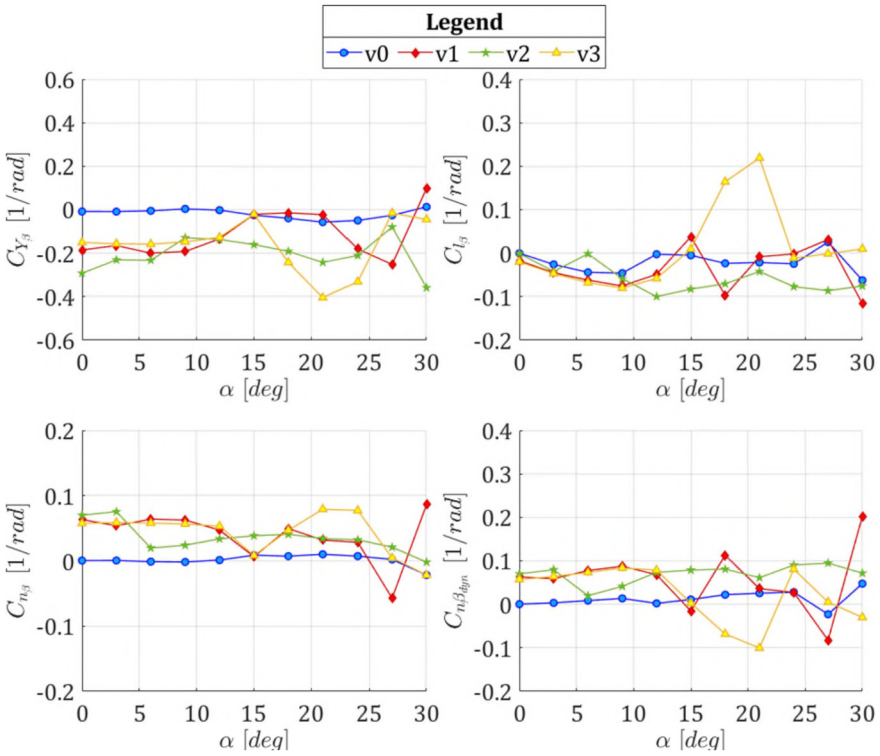

Fig. 14. Lateral and directional derivatives trend with angle of attack.

analysed frequency of 1.3 GHz is considered representative of long-range surveillance radar systems. Whilst this band is more typical of surface-based search, acquisition and Ground-Control-Intercept (GCI) radars, it has been historically used in AWACS (Airborne Warning & Control System), and more recently, it has found its way into air superiority platform designs (Sukhoi Su57 and Su75). On the other hand, the frequency of 9.6 GHz is considered representative of airborne fighter radars, Surface-Air-Missile (SAM) engagement radars, and a range of missile seekers (both surface-to-air and air-to-air).

Initially, the RCS of the baseline configuration is presented and discussed. Successively DRF charts, of the derived configurations, are analysed.

4.2.1. Baseline geometry RCS

The RCS maps of the baseline geometry were characterised by five main lobes (Fig. 16). These lobes were located at γ values of 26.5, 53, 90, 127, and 153.5 degrees. Note, the lobes at $\gamma = 53$ deg and $\gamma = 153.5$ deg were brightest and corresponded to the return of the planform's leading and trailing edges.

The lobes at $\gamma = 26.5$ deg and $\gamma = 127$ deg were a direct consequence of travelling waves from the wing trailing and leading edges respectively (see Fig. 17 for visual reference). Direct confirmation was sought by comparing HH (Fig. 16, left column) and VV (Fig. 16, right column) polarisations at low elevation angles ($\theta \leq 30$ deg). VV polarisation presented a return considerably higher (> 30 dB m^2) with respect to HH polarisation, for $\gamma = 26.5$ deg and $\gamma = 127$ deg, as, "for a planar wing, there is a strong return, in terms of travelling waves, due to opposite[3] edge excitation by the electric field component, perpendicular to wing's plane" [68]. Finally, the lobe located at $\gamma = 90$ deg resulted from the return generated from the wingtip. Away from the large magnitude lobes, the average RCS was exhibited in the interval between -35dB m^2 to -10 dB m^2 in the Lband and between -45 dB m^2 to -25 dB m^2 in the Xband. This resulted in excellent low-RCS characteristics for the baseline geometry. The principal difference between the Lband and Xband maps appeared in the rear quarter ($\gamma > 90$ deg), as demonstrated by the "A" label in Fig. 16. Local peaks appeared for $\gamma = 124$ deg, at $\theta = \pm 19$ deg and $\theta = \pm 30$ deg. Increasing or decreasing elevation angle caused the location of these peaks to smoothly vary their position in elevation, and magnitude value in terms of dB m^2. Such characteristics were associated with the additional return generated by the wingtips. Indeed, the wingtips electric size at Xband was 4.75 compared to a value of 0.5 for Lband. Here the additional return for the wingtips was only faintly noticeable in VV polarisation (Fig. 16, label "B").

4.2.2. DRF charts - lband

All derived airframes experienced a degradation in RCS, which was reflected in an increase in DRF. Configuration v_2 represented the worst case (Fig. 18, middle row). At both polarisations, range detection was increased by a factor of 3 to 8 in the interval of elevation angles between $\theta = -30$ deg to $\theta = 30$ deg, and azimuth between $\gamma = 26.5$ deg to $\gamma = 153.5$ deg. By contrast for configurations v_1 (Fig. 18, upper row) and v_3 (Fig. 18, lower row) these values of DRF (between 3 to 8), were observed for smaller ranges, that is elevation between $\theta = -27$ deg to $\theta = 27$ deg, and azimuth between $\gamma = 72$ deg to $\gamma = 153$ deg. Analysis of the maps also demonstrated additional lobes of increased return ($DFR > 1$). As shown from label "A" in Fig. 18, a high intensity lobe ($DFR = 6$) was present in both v_1 and v_3. This lobe was centred at $\gamma = 53$ deg and $\theta = 15$ deg and its appearance associated with the multipath bounce between empennage and wing surface. On the other hand, the increased return (DRF between 2 to 4) indicated by the label "B" in Fig. 18, represented the contribution to RCS generated by the trailing edge of the vertical tails.

Between elevations ranging from $\theta = -45$ to $\theta = -90$ and azimuth from $\gamma = 90$ deg to $\gamma = 153$, the empennages were no

[3] That is, wing's trailing edge if the airframe is illuminated from the front sector, and wing's leading edge if the airframe is illuminated from the rear sector.

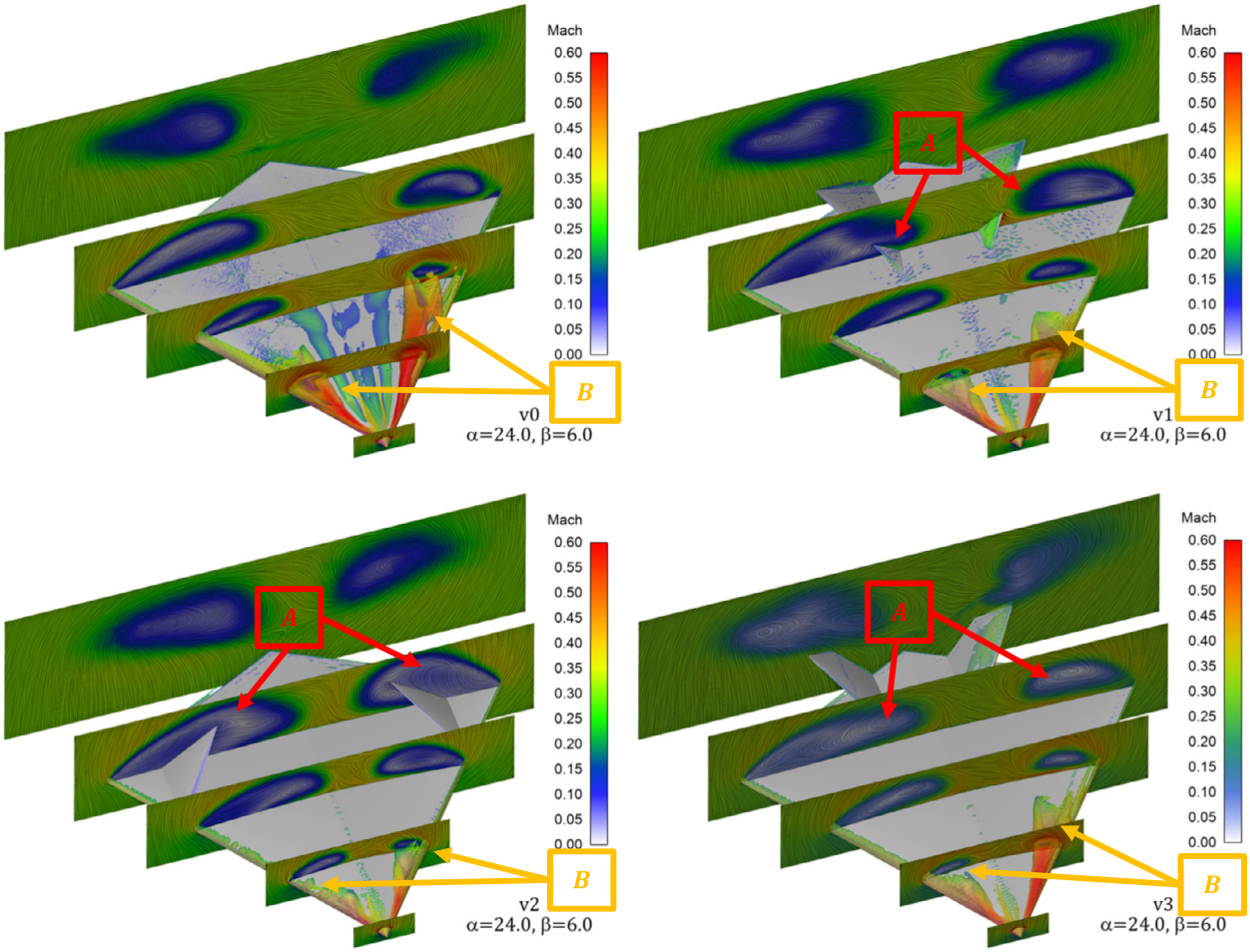

Fig. 15. Flow field comparison at $\alpha = 24$ deg, and $\beta = 6$ deg. Planar contours (at different longitudinal positions) of Mach number, and Iso-surface of vorticity. "A label": different interaction between windward and leeward vortex wake with relative vertical empennage. "B label": different vortex breakdown position between windward and leeward sides.

more shielded from illuminating rays coming from below and contributed to increasing RCS. By contrast, this was not observed in the front sector as the tails were obscured by the wing's surface and, indeed, here DRF was in the order of 1.5 or less (Fig. 18, label "D"). Additional features were observed at elevation angles above 60 deg. Here, as shown by label "C" in Fig. 18, DRF assumed values between 2 to 3. Again, the return was associated with the presence of vertical empennages.

It is of note that for azimuth angles below 26.5 deg, configurations v_1 and v_3 had DFR value of one, hence achieving the same RCS characteristics as the baseline geometry. The same was not true for configuration v_2.

4.2.3. DRF charts - Xband

RCS degradation observed in the Lband was qualitatively similar in the Xband. Again, all derived geometries experienced a strong increase in radar return (Fig. 19) when compared to the baseline geometry for elevation angles between $\theta = -30$ deg to $\theta = 30$ deg, and azimuth between $\gamma = 26.5$ deg to $\gamma = 153.5$ deg. DRF values observed were considerably higher (compared to L-band) and factors greater than 8 for large angular sectors were observed

As demonstrated in Fig. 19 (middle row), at both polarisations, extensive angular sectors experienced DRF values of more than 8, confirming the high signature characteristic of geometry v_2. Furthermore, even the front and rear quarters exhibited a consistent signature with a range increase factor between 3 to 5.

The characteristics of v_1 were considerably superior when compared to v_2. The extension of DRF values of more than 8 was notably inferior (Fig. 19, upper row). Additionally, geometry v_1 maintained the same RCS characteristics of the baseline geometry (i.e. $DRF = 1$) for azimuth angles less than 26.5. This area was further extended up to $\gamma = 70$ deg for negative elevation angles, as the vertical empennages were completely obscured by the wing profile at these attitudes (Fig. 19, label "A"). Conversely, the same was not true for the rear quarter of the airframe where DFR had an average value of 3, with minor lobes having values as high as 6 (Fig. 19, label "B"). For positive elevation angles of greater than 30 deg, the signature was once again increased due to the introduction of the tails. Here, in a similar manner to the bottom-rear part of the map, DFR attained an average value of 3 with small peaks up to 6 (Fig. 19, label "C"). Qualitatively configuration v_3 exhibited a DFR map to v_1 (Fig. 19, lower row). Minor differences were observed in the region of high return (beam and rear quarter aspects, at low elevation angles), as shown by label "D" of Fig. 19.

For configuration v_3, the extension of the area with $DRF \geq 8$ was less when compared to geometry v_1. This aspect was correlated to the size difference between the vertical tails in the two geometries, where v_3 empennages were slightly smaller (see Fig. 2). An additional difference was the appearance of a high return lobe in the v_3 map, centred at $\gamma = 53$ deg and $\theta = -75$ deg (Fig. 19, label "E"). This was related to the trailing edge of the tails being directly visible at these attitudes. This feature was more apparent in HH polarisation ($DRF = 3$) than in VV polarisation ($DRF = 2$).

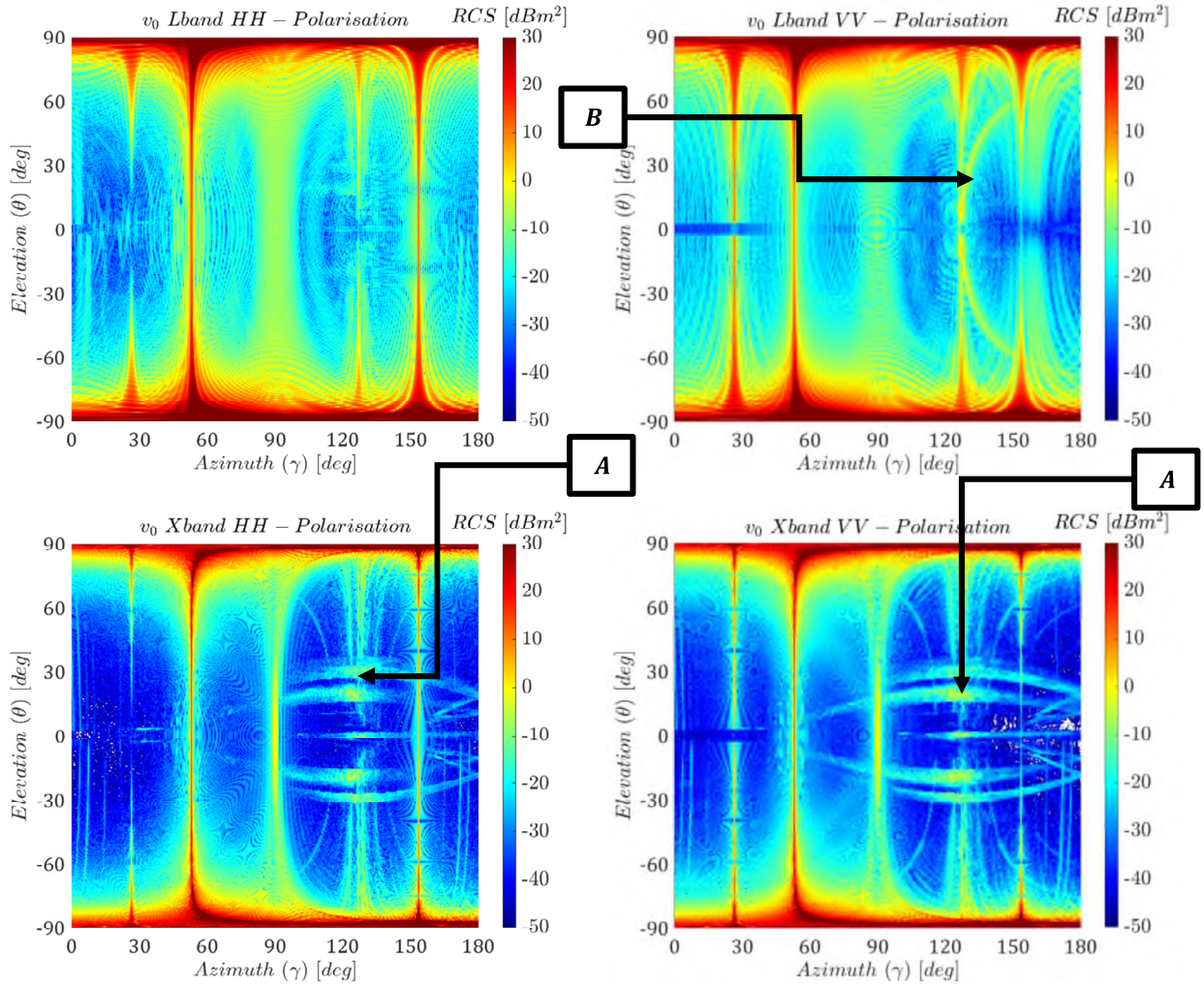

Fig. 16. RCS maps of baseline geometry.

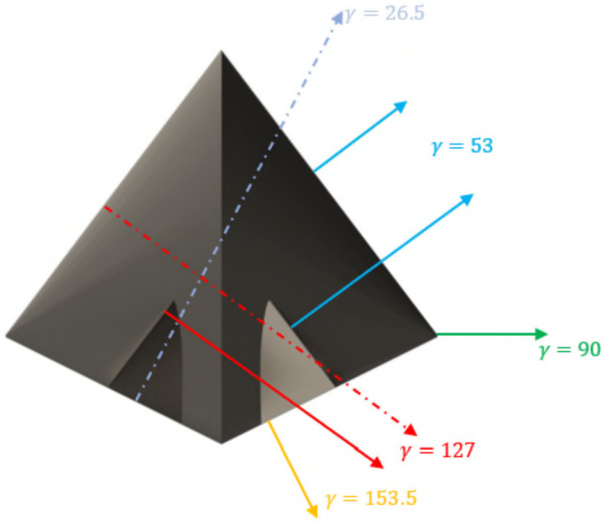

Fig. 17. Angles of large lobes in the RCS pattern at zero elevation. Plot relative to v_1 configuration.

4.3. Trade-off analysis

As anticipated, the aerodynamic and radar signature requirements were in contrast to one another. Aerodynamically, the analysis demonstrated that configuration v_2 provided adequate lateral/directional performance, however, it suffered considerably in terms of RCS deterioration.

Conversely, configurations v_1 and v_3 offered a good compromise between the required signature and aerodynamic performance. Configuration v_1 was able to attain adequate spin/departure resistance behaviour across the majority of the flight conditions assessed. Where the azimuth angle was below 26.5 deg (front aspect), the detection rate was not observed to deteriorate when compared to the baseline geometry. Configuration v_3 had similar RCS characteristics to v_1, although worse performance was observed in spin/departure characteristics, especially at angles of attack above 18 deg. Consequently, $v1$ demonstrated the optimum compromise between the signature and aerodynamic characteristics and is identified as being the geometry most warranting further investigation. Such work would include a relocation of the vertical empennages to avoid their potential disruptive interference within the main vortices of the wings and to further improve spin/departure characteristics during combat engagements.

4.4. Discussion

The combined computational fluid dynamics and electromagnetic analyses of the configurations permitted an initial qualitative assessment of the trade-off between controllability (in the lateral/directional channel) and survivability (in terms of radar signature control/suppression). The most significant findings are summarised below:

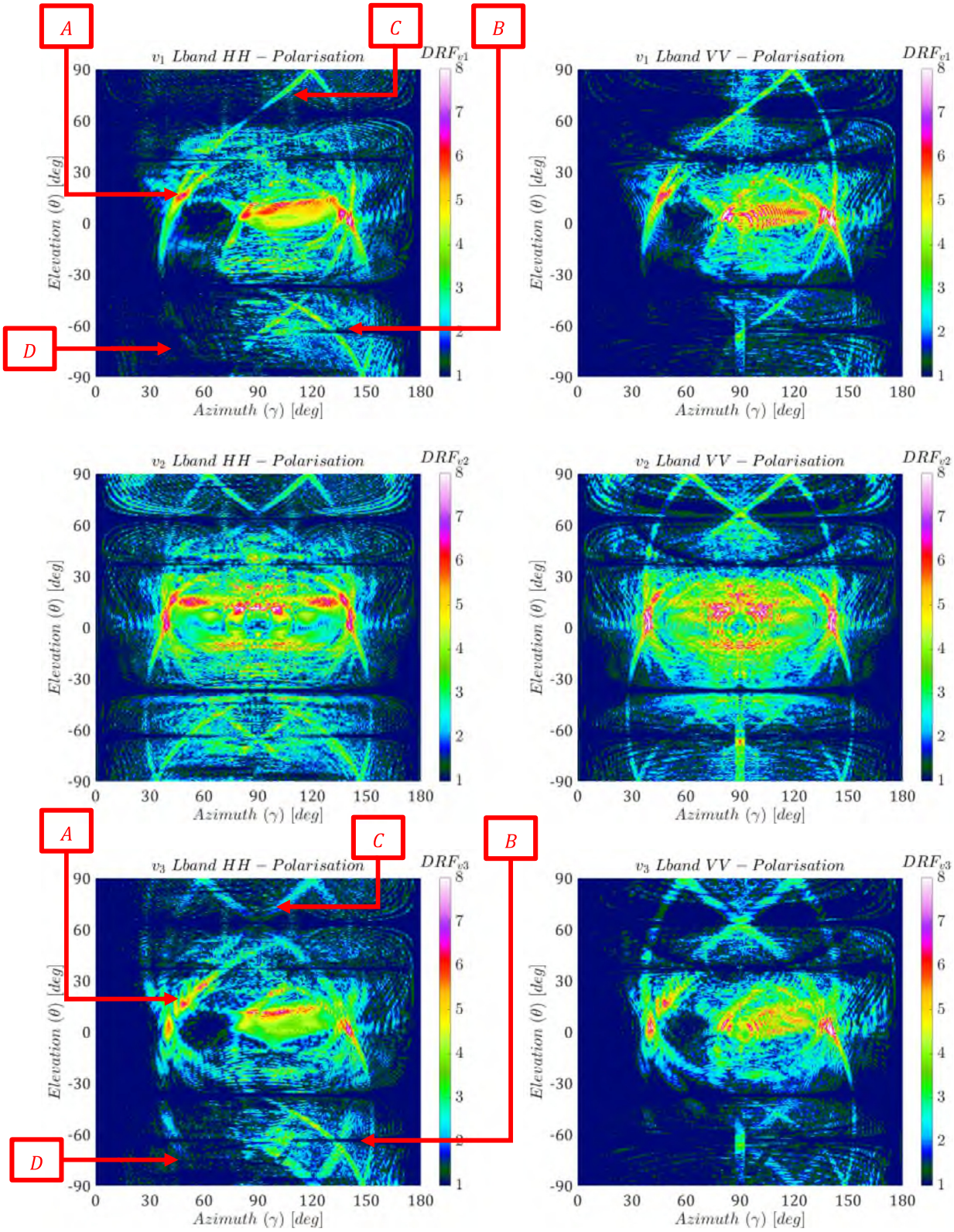

Fig. 18. Computed DRF for derived airframes. Lband. HH polarisation (left column) and VV polarisation (right column). Label A: lobe generated by multipath bounce between empennage and wing surface. Label B: return generated by vertical tail trailing edge seen from beneath wing plane. Label C: return generated by empennage inclined surface. Label D: low DRF area due to wing shielding of vertical empennages.

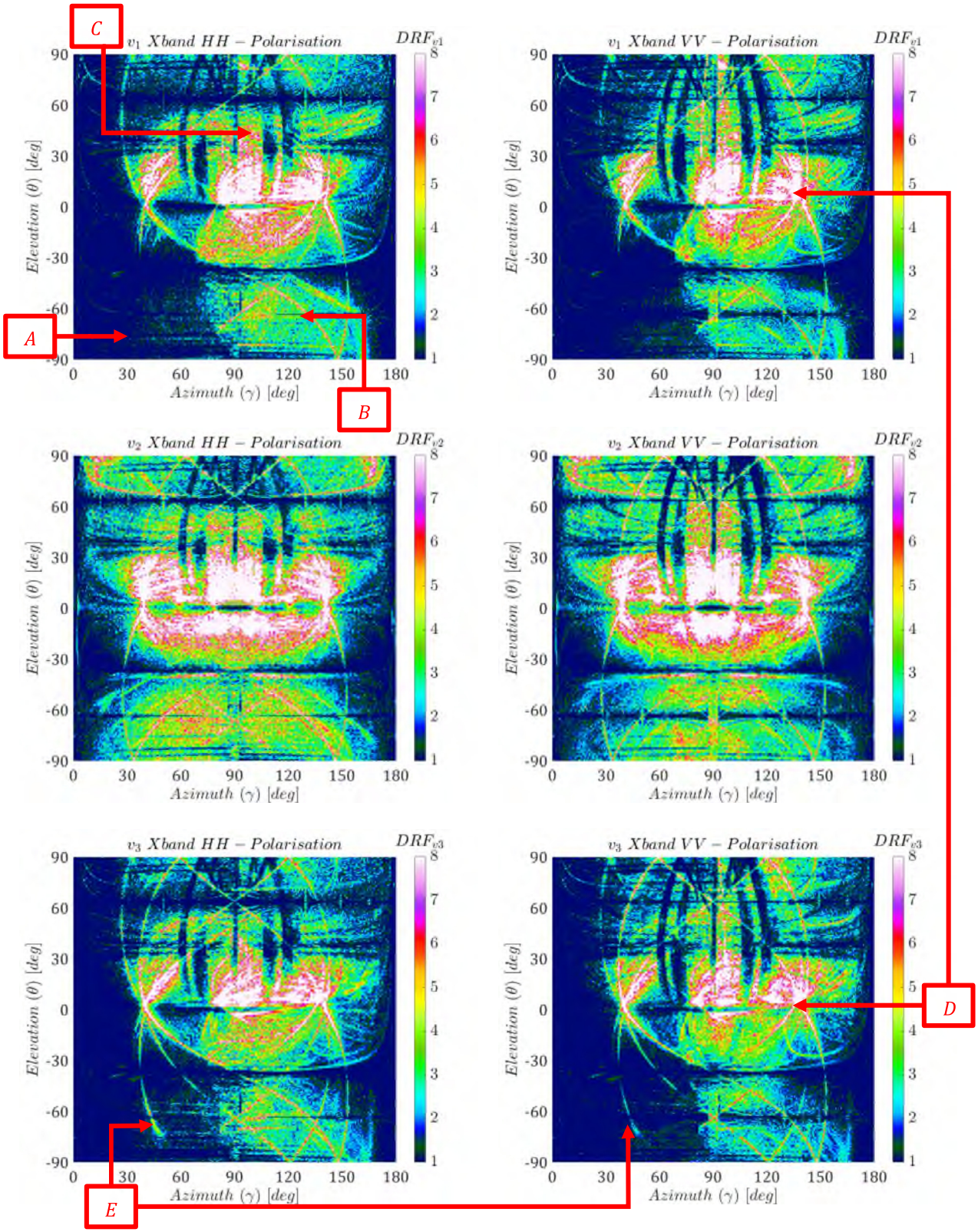

Fig. 19. Computed DRF for derived airframes. Xband. HH polarisation (left column) and VV polarisation (right column).

- The baseline geometry, whilst achieving excellent low RF signature characteristics, was not an adequate design for air superiority. Its poor spin/departure resistance characteristics would necessitate significant effort in control surfaces/mechanisms at angles of attack typical of air-to-air combat. This would ultimately result in less control power for manoeuvring, thus limiting combat capability.
- The adoption of vertical empennages degraded RCS, especially in side-facing aspects where range detection would increase by a factor of 6 in Lband and 8 in Xband. Configuration v_1 and v_3 exhibited reduced signature deterioration when compared to v_2. It was also found that a tail arrangement as per the v_1 with optimally positioned tails would not affect the frontal signature, especially when the airframe is illuminated from underneath.
- Although, the placement of tails improved departure resistance, at some specific angles of attack (>18 deg), configurations v_1 and v_3 experienced a sudden loss of directional/lateral characteristics due to adverse effects of the wings' wake on the empennages, limiting the maximum usable lift coefficient.

The general finding was that, for the configurations explored, there was a direct dependence between the increase of lateral/directional controllability and the decrease of pure-geometric signature suppression characteristics. Such information is critical in the initial design phase of a modern combat aircraft, permitting the quantification of loss or gain in performance (manoeuvrability, controllability, radar susceptibility) and tailoring the subsequent design iteration to the specifics of the project (i.e. the principal mission of the airframe). The ability to quantify the mutual interference between different design requirements is pivotal for the correct design of combat airframes, and since RCS requirement is a mandatory aspect for novel projects, prior knowledge of the impact on aerodynamics (as well as on other physical aspects) is crucial.

5. Conclusions

The study confirmed the difficulties encountered in air superiority aircraft design upon integrating the RCS requirements and proper spin/departure characteristics at high angles of attack. It was demonstrated that it is possible to obtain sufficient lateral/directional characteristics without an significant deterioration of the radar signature. The study also verified the potential to quantify - during the initial design phase of a combat aircraft - the level of mutual interference between RCS reduction requirements and departure resistance, aspects that conflict with modern design, where there is the tendency to reduce (or even eliminate) the vertical empennages.

The overall analysis indicated that the optimal configuration would utilise the adoption of the v_1 typology of vertical empennages. In this configuration, vertical tail planform was fully inscribed inside wing one, partially shielding them when illuminated from below. This configuration was capable of achieving the BW-chart desired class "A" at angles of attack up to 18 deg. Further improvement in spin/departure characteristics could be achieved by decoupling the wing vortex system from the tail. Aerodynamic analyses indicated that the loss of lateral/directional stability at the highest angles of attack was related to the impact of the low-energy wake of wing vortices with the tail, thereby reducing its effectiveness.

Of course, it should be noted that the above conclusions hold only for the baseline wing geometry studied in this paper (AVT-183). The specific values will change with the wing planform. However, these conclusions provide some reference values that may help combat aircraft designers. It is suggested that future studies could analyse the effects of the adoption of Radar Absorbing Material (RAM) coatings on surfaces. Additionally, proposed geometries should be analysed in the transonic and supersonic regime, which for an air-superiority design, are also part of the combat envelope. After these stages are completed, a new generation of vertical empennages could be derived, and a study could be conducted to derive additional data on how to address the design challenges.

Declaration of competing interest

The authors declare that they have no known competing financial interests or personal relationships that could have appeared to influence the work reported in this paper.

Data availability

Data will be made available on request.

Acknowledgements

The authors would like to thank Dr Alexander Murray (Department of Engineering Science – University of Oxford) for his contribution and suggestions on reviewing the paper.

References

[1] B. Tamrat, Fighter aircraft agility assessment concepts and their implication on future agile fighter design, in: Aircraft Design, Systems and Operations Meeting, 1988, pp. 1–12, https://doi.org/10.2514/6.1988-4400.
[2] R.K. Liefer, J. Valasek, D.P. Eggold, D.R. Downing, Fighter agility metrics, research and test, J. Aircr. 29 (3) (1992) 452–457, https://doi.org/10.2514/3.46182.
[3] B. Tamrat, Flight path/nose pointing - a required criterion in future fighter aircraft design, in: 10th Atmospheric Flight Mechanics Conference, 1983, pp. 1–5, https://doi.org/10.2514/6.1983-2123.
[4] J. Stillion, Trends in air-to-air combat: implications for future air superiority, CSBA Rep. (2015).
[5] J. Bronk, Russian and Chinese Combat Air Trends: Current Capabilities and Future Threat Outlook, London, Oct. 2020.
[6] AGARD-CP-319, Combat Aircraft Manoeuvrability, 1981.
[7] R.F. Stengel, P.W. Berry, Stability and control of maneuvering high-performance aircraft, J. Aircr. 14 (8) (Aug. 1977) 787–794, https://doi.org/10.2514/3.58854.
[8] J.E. Cochran, C.-S. Ho, G.A. Castleberry, Stability of asymmetric equilibrium flight states, J. Aircr. 19 (9) (Sep. 1982) 705–706, https://doi.org/10.2514/3.61547.
[9] AGARD-R-815, Loads and Requirements for Military Aircraft, 1996.
[10] AGARD-AG-234, Active Controls in Aircraft Design, 1978.
[11] P. Stojakovic, B. Rasuo, Minimal safe speed of the asymmetrically loaded combat airplane, Aircr. Eng. Aerosp. Technol. 88 (1) (Jan. 2016) 42–52, https://doi.org/10.1108/AEAT-03-2014-0033.
[12] Assessment of Stability and Control Prediction Methods for NATO Air and Sea Vehicles, Apr. 2012.
[13] Extended Assessment of Stability and Control Prediction Methods for NATO Air Vehicles, Nov. 2016.
[14] R.M. Cummings, A. Schütte, A. Hübner, Overview of stability and control estimation methods from NATO STO task group AVT-201, in: 51st AIAA Aerospace Sciences Meeting Including the New Horizons Forum and Aerospace Exposition 2013, 2013, https://doi.org/10.2514/6.2013-968.
[15] A. Jirásek, R.M. Cummings, A. Schütte, K. Huber, The NATO STO AVT-201 task group on extended assessment of stability and control prediction methods for NATO air vehicles: summary, in: 32nd AIAA Applied Aerodynamics Conference, 2014, https://doi.org/10.2514/6.2014-2394.
[16] K.C. Huber, D.D. Vicroy, A. Schuette, A. Huebner, UCAV model design and static experimental investigations to estimate control device effectiveness and S&C capabilities, in: 32nd AIAA Applied Aerodynamics Conference, American Institute of Aeronautics and Astronautics, 2014, https://doi.org/10.2514/6.2014-2002.
[17] A. Schütte, K.C. Huber, N.T. Frink, O.J. Boelens, Stability and control investigations of generic 53 degree swept wing with control surfaces, J. Aircr. 55 (2) (Mar. 2016) 502–533, https://doi.org/10.2514/1.C033700.
[18] M. Ghoreyshi, M.E. Young, A.J. Lofthouse, A. Jirásek, R.M. Cummings, Numerical simulation and reduced-order aerodynamic modeling of a lambda wing configuration, J. Aircr. 55 (2) (Jun. 2016) 549–570, https://doi.org/10.2514/1.C033776.

[19] J. Coppin, T. Birch, D. Kennett, G. Hoholis, K. Badcock, Prediction of control effectiveness for a highly swept unmanned air vehicle configuration, J. Aircr. 55 (2) (Oct. 2016) 534–548, https://doi.org/10.2514/1.C033988.
[20] D. Zimper, D. Hummel, Analysis of the transonic flow around a unmanned combat aerial vehicle configuration, J. Aircr. 55 (2) (Mar. 2016) 571–586, https://doi.org/10.2514/1.C033697.
[21] M. Rein, J. Irving, G. Rigby, T.J. Birch, High speed static experimental investigations to estimate control device effectiveness and S&C capabilities, in: 32nd AIAA Applied Aerodynamics Conference, American Institute of Aeronautics and Astronautics, 2014, https://doi.org/10.2514/6.2014-2004.
[22] C.M. Liersch, R.M. Cummings, A. Schütte, NATO STO/AVT-251: a joint exercise in collaborative combat aircraft design, in: Specialists' Meeting on Multidisciplinary Design Approaches and Performance Assessment of Future Combat Aircraft, Sep. 2020, pp. 1–18.
[23] A. Schuette, J. Vormweg, R.G. Maye, T. Jeans, Aerodynamic shaping design and vortical flow design aspects of a 53 deg swept flying wing configuration, in: 2018 Applied Aerodynamics Conference, American Institute of Aeronautics and Astronautics, 2018, https://doi.org/10.2514/6.2018-2841.
[24] A. Schütte, D. Hummel, S.M. Hitzel, Flow physics analyses of a generic unmanned combat aerial vehicle configuration, J. Aircr. 49 (6) (Nov. 2012) 1638–1651, https://doi.org/10.2514/1.C031386.
[25] C.M. Liersch, A. Schütte, M. Siggel, J. Dornwald, Design studies and multidisciplinary assessment of agile and highly swept flying wing configurations, CEAS Aeronaut. J. 11 (3) (2020) 781–802, https://doi.org/10.1007/s13272-020-00453-y.
[26] P. Loechert, K.C. Huber, C. Liersch, A. Schuette, Control device studies for yaw control without vertical tail plane on a 53° swept flying wing configuration, in: 2018 Applied Aerodynamics Conference, American Institute of Aeronautics and Astronautics, 2018, https://doi.org/10.2514/6.2018-3329.
[27] A.H. Stadmore, Radar cross section fundamentals for the aircraft designer, in: Aircraft Systems and Technology Meeting, 1979.
[28] V. Hoang, P.C. Van Dam, A.H. Dwyer, Shape optimisation for aerodynamic efficiency and low observability, in: AIAA Fluid Dynamics Conference, 1993.
[29] H. Vinh, C.P. van Dam, H.A. Dwyer, Airfoil shaping for reduced radar cross section, J. Aircr. 31 (4) (1994) 787–793, https://doi.org/10.2514/3.46562.
[30] D. Lee, L.F. Gonzalez, K. Srinivas, D. Auld, K.C. Wong, Aerodynamic/RCS shape optimisation of unmanned aerial vehicles using hierarchical asynchronous parallel evolutionary algorithms, in: 24th AIAA Applied Aerodynamics Conference, 2006, https://doi.org/10.2514/6.2006-3331.
[31] D. Wu, T. Long, Y. Li, M. Jiang, B. Huang, Aero-structure-stealth coupled optimization for high aspect ratio wing using adaptive metamodeling method, in: 15th AIAA/ISSMO Multidisciplinary Analysis and Optimization Conference, 2014, https://doi.org/10.2514/6.2014-2304.
[32] H. Tianyuan, Y. Xiongqing, Aerodynamic/stealthy/structural multidisciplinary design optimization of unmanned combat air vehicle, Chin. J. Aeronaut. 22 (4) (2009) 380–386, https://doi.org/10.1016/S1000-9361(08)60114-4.
[33] H.E. Taha, M.R. Hajj, Optimization of aerodynamic performance and stability of a stealth aircraft, in: 54th AIAA/ASME/ASCE/AHS/ASC Structures, Structural Dynamics, and Materials Conference, 2013, https://doi.org/10.2514/6.2013-1674.
[34] Y. Pan, J. Huang, F. Li, C. Yan, Integrated design optimization of aerodynamic and stealthy performance for flying wing aircraft, in: Proceedings of the International MultiConference of Engineers and Computer Scientists 2017, vol. II, 2017.
[35] A. Papageorgiou, M. Tarkian, K. Amadori, J. Ölvander, Multidisciplinary optimization of unmanned aircraft considering radar signature, sensors, and trajectory constraints, J. Aircr. 55 (4) (2018) 1629–1640, https://doi.org/10.2514/1.C034314.
[36] M. Li, J. Bai, L. Li, X. Meng, Q. Liu, B. Chen, A gradient-based aero-stealth optimization design method for flying wing aircraft, Aerosp. Sci. Technol. 92 (2019) 156–169, https://doi.org/10.1016/j.ast.2019.05.067.
[37] L. Zhou, J. Huang, Z. Gao, W. Zhang, Three-dimensional aerodynamic/stealth optimization based on adjoint sensitivity analysis for scattering problem, AIAA J. 58 (6) (2020) 2702–2715, https://doi.org/10.2514/1.J059136.
[38] M. Li, J. Chen, X. Feng, F. Qu, J. Bai, An efficient adjoint method for the aero-stealth shape optimization design, Aerosp. Sci. Technol. 118 (2021) 107017, https://doi.org/10.1016/j.ast.2021.107017.
[39] S. Shao, G. Jia, P. Yin, Z. Hou, L. Zhang, Z. Guo, Trailing-edge jets for UCAV's flight control over a wide speed range, Aerosp. Sci. Technol. (2022) 107788, https://doi.org/10.1016/j.ast.2022.107788.
[40] J. Luckring, O. Boelens, A unit-problem investigation of blunt leading-edge separation motivated by AVT-161 SACCON research, in: RTO-MP-AVT-189 Meeting, Portsmouth, 2012.
[41] S.M. Hitzel, O.J. Boelens, M. Rooij, A. Hövelmann, Vortex development on the AVT-183 diamond wing configuration – numerical and experimental findings, Aerosp. Sci. Technol. 57 (Oct. 2016) 90–102, https://doi.org/10.1016/j.ast.2015.12.007.
[42] R. Whitford, Design for Air Combat, Jane's, 1987.
[43] B.F. Tamrat, The X-31: a post-stall technology (PST) fighter close-in-combat results assessment, and a look at new CIC performance evaluation metrics, in: Collection of Technical Papers - AIAA Atmospheric Flight Mechanics Conference, vol. 2, Jun. 2004, pp. 1002–1022, https://doi.org/10.2514/6.2004-5173.
[44] O.J. Boelens, et al., Numerical and theoretical considerations for the design of the AVT-183 diamond-wing experimental investigations (invited), in: 53rd AIAA Aerospace Sciences Meeting, 2015, https://doi.org/10.2514/6.2015-0062.
[45] A. Hövelmann, F. Knoth, C. Breitsamter, AVT-183 diamond wing flow field characteristics part 1: varying leading-edge roughness and the effects on flow separation onset, Aerosp. Sci. Technol. 57 (Oct. 2016) 18–30, https://doi.org/10.1016/j.ast.2016.01.002.
[46] J. Roskam, Airplane design part VII: determination of stability, in: Control and Performance Characteristics: FAR and Military Requirements. Design and Analysis Research Corporation, Kansas, USA, 1986.
[47] D. Raymer, Aircraft Design: A Conceptual Approach, 6th edition, AIAA Educational Series, 2018.
[48] K. Huenecke, Modern Combat Aircraft Design, Naval Institute Press, Annapolis, United States, 1987.
[49] D. Howe, Aircraft Conceptual Design Synthesis, Professional Engineering Publishing Ltd, London, United Kingdom, 2000.
[50] D.R. Schaufele, The Elements of Aircraft Preliminary Design, Aries Publications, California, United States, 2007.
[51] L. Nicolai, G. Carichhner, Fundamental of Aircraft and Airship Design Volume I: Aircraft Design, AIAA Educational Series, 2010.
[52] J. Roskam, Airplane design part V: component weight estimation, in: Design and Analysis Research Corporation, Kansas, USA, 1985.
[53] F.R. Menter, R. Lechner, A. Matyushenko, Best Practice: Generalized k-w Two-Equation Turbulence Model in ANSYS CFD (GEKO), 2019.
[54] P.E. Smirnov, F.R. Menter, Sensitization of the SST turbulence model to rotation and curvature by applying the Spalart–Shur correction term, J. Turbomach. 131 (4) (2009), https://doi.org/10.1115/1.3070573.
[55] M.M. Tomac, A.W. Rizzi, CFD study of vortex separation phenomena on blunt diamond wing, in: 53rd AIAA Aerospace Sciences Meeting, 2015, https://doi.org/10.2514/6.2015-0291.
[56] N.T. Frink, Numerical analysis of incipient separation on 53-deg swept diamond wing, in: 53rd AIAA Aerospace Sciences Meeting, 2015, https://doi.org/10.2514/6.2015-0288.
[57] M. Ghoreyshi, K. Ryszka, R.M. Cummings, A.J. Lofthouse, Vortical flow prediction of a diamond wing with rounded leading edges, Aerosp. Sci. Technol. 57 (Oct. 2016) 103–117, https://doi.org/10.1016/j.ast.2016.02.011.
[58] R.J. Boyd, Aerial Attack Study, 1964.
[59] R.L. Shawn, Fighter Combat: Tactics and Manoeuvring, Naval Institute Press, Annapolis, Maryland, 1986.
[60] J. Rom, High Angle of Attack Aerodynamics, Springer, New York, NY, 1992, https://doi.org/10.1007/978-1-4612-2824-0.
[61] C. Christmann, D. Kiehn, M. Stradtner, C.M. Liersch, Initial assessment of stability and controllability in the early stage of combat aircraft design, in: DLRK, Jan. 2023 [Online]. Available: https://elib.dlr.de/189426/.
[62] H. John, W. Krauss, High angle of attack characteristics of different fighter configurations, MBB UFE 1443 (1978).
[63] A.C. Woo, H.T.G. Wang, M.J. Schuh, M.L. Sanders, EM programmer's notebook-benchmark radar targets for the validation of computational electromagnetics programs, IEEE Antennas Propag. Mag. 35 (1) (1993) 84–89, https://doi.org/10.1109/74.210840.
[64] T.W. Hamilton, Manoeuver Limitations of Combat Aircraft, 1979, AGARD-AR-155A.
[65] H. Douglas Greer, Summary of Directional Divergence Characteristics of Several High-Performance Aircraft Configurations, Langley Research Center, 1972.
[66] W. Bihrle, B. Barnhart, Design Charts and Boundaries for Identifying Departure Resistant Fighter Configurations, Naval Air Development Center - NADC-76154-30, Washington, 1978.
[67] T.L. Nguyen, J.V. Foster, Development of a Preliminary High-Angle-of-Attack Nose-Down Pitch Control Requirement for High-Performance Aircraft, Hampton, Virginia, 1990.
[68] F.E. Knott, F.J. Shaeffer, T.M. Tuley, Radar Cross Section, SciTech Publishing Inc., Boston, USA, 2004.
[69] S.P. Fears, H.M. Ross, T.M. Moul, Low-speed wind-tunnel investigation of the stability and control characteristics of a series of flying wings with sweep angles of 50 deg, http://ntrs.nasa.gov/archive/nasa/casi.ntrs.nasa.gov/19950023805.pdf, 1995. (Accessed 10 August 2022).
[70] T.M. Moul, S.P. Fears, H.M. Ross, J.V. Foster, Low-speed wind-tunnel investigation of the stability and control characteristics of a series of flying wings with sweep angles of 60°, [Online]. Available, http://techreports.larc.nasa.gov/ltrs/ltrs.html, 1995. (Accessed 10 August 2022).
[71] H.M. Ross, S.P. Fears, T.M. Moul, Low-speed wind-tunnel investigation of the stability and control characteristics of a series of flying wings with sweep angles of 70°, [Online]. Available, http://techreports.larc.nasa.gov/ltrs/ltrs.html, 1995. (Accessed 10 August 2022).
[72] J. Johnson jr., S. Grafton, L. Yip, Exploratory investigation of the effects of vortex bursting on the high angle-of-attack lateral-directional stability characteristics of highly-swept wings, in: 11th Aerodynamic Testing Conference, American Institute of Aeronautics and Astronautics, 1980, https://doi.org/10.2514/6.1980-463.

https://dspace.org/

A trade-off analysis between lateral/directional stability and radar cross section requirements of an air-to-air combat airframe

Bacci, David; Vagias, Ioannis

2023-05-09
Elsevier
https://doi.org/10.1016/j.ast.2023.108361
Bacci D, Vagias I. (2023) A trade-off analysis between lateral/directional stability and radar cross section requirements of an air-to-air combat airframe, Aerospace Science and Technology, Volume 138, July 2023, Article number 108361

Downloaded from a DSpace repository. https://dspace.org/